AUTOMATIC BRAIN MR IMAGE SEGMENTATION BY RELATIVE THRESHOLDING AND MORPHOLOGICAL IMAGE ANALYSIS

Kai Li, Allen D. Malony
Department Of Computer and Information Science University of Oregon
1202 University of Oregon, Eugene, OR 97403 USA

Don M. Tucker
Electrical Geodesics, Inc.
Riverfront Research Park, 1600 Millrace Drive, Suite 307, Eugene, OR 97403 USA

Keywords: Segmentation, brain, MR, intensity inhomogeneity, relative thresholding, mathematical morphology, skeleton-based opening, geodesic opening, *a priori* knowledge, first-order logic.

Abstract: We present an automatic method for segmentation of white matter, gray matter and cerebrospinal fluid in T1-weighted brain MR images. We model images in terms of spatial relationships between near voxels. Brain tissue segmentation is first performed with relative thresholding, a new segmentation mechanism which compares two voxel intensities against a relative threshold. Relative thresholding considers structural, geometrical and radiological *a priori* knowledge expressed in first-order logic. It makes intensity inhomogeneity transparent, avoids using any form of regularization, and enables global searching for optimal solutions. We augment relative thresholding mainly with a series of morphological operations that exploit *a priori* knowledge about the shape and geometry of brain structures. Combination of relative thresholding and morphological operations dispenses with the prior skull stripping step. Parameters involved in the segmentation are selected based on *a priori* knowledge and robust to inter-data variations.

1 INTRODUCTION

Image segmentation of brain magnetic resonance (MR) images, particularly T1-weighted MR images, has found wide applications ranging from morphometric or functional studies to neurosurgical planning. Some brain MR image segmentation methods aim at labeling voxels with different brain tissue types. Typically, the tissue types of interest are white matter (WM), gray matter (GM) and cerebrospinal fluid (CSF). Based upon the voxel classification, we can reconstruct some particular brain structures, such as the outer and inner cortical surfaces. Some segmentation procedures directly aim at the extraction of cortical surfaces. These two goals roughly correspond to two different categories of dominant segmentation methods in brain image segmentation: voxel classification methods based on the intensity of image voxels and deformable model-based methods considering structural information derived from the image.

Traditional voxel classification methods such as Expectation-Maximization (EM) and fuzzy c-means clustering are problematic in the presence of intensity inhomogeneity (IIH). IIH, also referred to as bias field, is an image artifact induced by a number of factors in image acquisition and perceived as a smooth variation of intensity across the spatial domain of the image. IIH correction is often performed as a preprocessing step (Sled et al., 1998; Cohen et al., 2000) or proceeds simultaneously with voxel classification (Pham and Prince, 1999; Ahmed et al., 2002; Wells et al., 1998). Brain MR image segmentation based on deformable models (MacDonald et al., 2000; Zeng et al., 1999; Xu et al., 1999) tracks cortical surfaces by exploiting information derived from the image, typically edges, together with *a priori* knowledge about the location, geometry, and even shape of these surfaces. These methods usually involve minimization of an object function that attempts to fit the model to the image data with the regularization typically on the surface smoothness.

Automation robustness of these segmentation methods is not satisfactory yet mainly due to three reasons. First, a common disadvantage of these methods is that their performance depends on the initial segmentation state and is prone to be trapped in local optima. Second, in those methods with regularization involved, one or more parameters that control the relative importance of regularization often have to be empirically selected for each input image and

Li K., D. Malony A. and M. Tucker D. (2006).
AUTOMATIC BRAIN MR IMAGE SEGMENTATION BY RELATIVE THRESHOLDING AND MORPHOLOGICAL IMAGE ANALYSIS.
In *Proceedings of the First International Conference on Computer Vision Theory and Applications*, pages 354-361
DOI: 10.5220/0001366103540361
Copyright © SciTePress

may be sensitive to inter-data variations. This is the case in the regularization of surface smoothness in deformable model-based methods and regularization of the IIH variation smoothness in some voxel classification methods. Third, some brain tissue segmentation methods require a prior step of skull stripping, which by itself is a difficult problem for complete automation (Rehm et al., 04).

W present a brain T1-weighted MR image segmentation method using relative thresholding (RT) and morphological operations that aims to improve automation robustness in all three aspects described above. Relative thresholding is based on image modeling in terms of local spatial relationships between near voxels and exploits structural, geometrical and radiological *a priori* knowledge expressed in first-order logic. RT makes the IIH problem transparent, avoids using any form of regularization, and enables global searching for optimal solutions. Results from relative thresholding are improved mainly using a series of morphological operations. The major two morphological operations are what we refer to as skeleton-based opening and geodesic opening. They are designed to robustly remove unwanted structures from brain structures motivated by the *a priori* knowledge about their special shape and geometry. Parameters involved in the segmentation are selected based on *a priori* knowledge and robust to inter-data variations. The combination of RT and morphological operations dispenses with the prior skull stripping step.

The paper is organized as follows. We first give some basic definitions in section 2. RT and the two morphological operations are presented in section 3 and 4 respectively. The whole segmentation pipeline is described in section 5. The results are presented in section 6 and the paper concludes in section 7.

2 DEFINITIONS

We first define some terms used throughout the paper. A 3D image can be viewed as a set of cubes structured regularly, where each cube represents a volumetric pixel (*voxel*). Each voxel v has three types of neighbors: 6 *face neighbors*, 12 *edge neighbors* and 6 *point neighbors* that share a face, an edge, or a point with v respectively.

The 6 face neighbors are regarded as connected to the central voxel v in *6-connectivity* and form the *6-neighborhood* $\mathcal{N}^6(v)$ of v. The 6 face neighbors and the 12 edge neighbors form the *18-neighborhood* $\mathcal{N}^{18}(v)$ (*18-connectivity*). Finally all 26 neighbors form the *26-neighborhood* $\mathcal{N}^{26}(v)$ (*26-connectivity*).

Corresponding to the three types of connectivity, three types of distance between two voxels, D^6, D^{18}, and D^{26}, are defined as the number of steps in the minimal path between the two voxels. Finally, we define a *grid graph* from an image taking each voxel as a vertex and adding edges in terms of one of the connectivies between voxels.

3 RELATIVE THRESHOLDING

Relative thresholding is characterized as differentiating the labels of near voxels by comparing their intensities with respect to a relative threshold. RT exploits various *a priori* knowledge in terms of a critical data structure which we refer to as *gradient graph*, and is justified by image modeling based on the spatial constraints on the intensities of near voxels. Optimal relative thresholds are found with a trial-and-evaluation scheme.

3.1 *A Priori* Knowledge

Let $\vec{g} = \nabla g(\sigma_\nabla)$ be the gradient vector image of $g(\sigma_\nabla)$. Throughout this paper, we use $g(\sigma)$ to denote the result image of performing Gaussian filtering with standard deviation σ on the input image y. We construct a directed graph $G = (V, E)$ from $\vec{g}$ such that each vectex $v_i \in V$ corresponds to the voxel x_i in a region of interest R and each directed edge $e_i \in E$ emanates from v_i to v_j, where v_j is the one of v_i's 26-neighbors that is in the direction of the gradient vector $\vec{g}_i$. When v_j is outside R, e_i is forced to be a loop from v_i to itself.

The structural, geometrical and radiological *a priori* knowledge that we use in RT is:

- K_1: CSF, GM, and WM are organized as a layered structure from outside to inside;
- K_2: The average intensities of CSF, GM, and WM are in ascending order in T1-weighted MR images.
- K_3: The cortex thickness is nearly uniform;

Based on the gradient graph, this *a priori* knowledge is formulated as the following first-order logic: There exist a suitable σ_∇ and p such that:

- For each GM voxel v_i, there is a path in G of length p from v_i to a WM voxel;
- For each CSF voxel v_i adjacent to GM, there is a path in G of length $\leq p$ from v_i to a GM voxel;
- There is no path from a WM voxel to a non-WM voxel in G;
- There is no path from any non-brain voxels to WM in G without passing CSF.

3.2 Image Modeling

We model images in terms of the spatial relationships between voxels instead of as statistical distributions

on the absolute voxel intensities. Our intuition is that if the segmentation task is not beyond the human recognition capability, near voxels of the same type should possess less difference in intensity with respect to that of near voxels of different types. With this type of image modeling, we attempt to avoid the limitation imposed by the form of statistical distributions and provide a framework for introducing various *a priori* knowledge into the segmentation task.

Suppose that there are K voxel types among a total of N voxels in the space domain Ω, which represents either the whole image or a region of interest in the image. In brain MR image segmentation, K typically equals to 3 and the three tissues of interest are CSF, GM and WM. Let the coordinates of voxels be x_i, $1 \leq i \leq N$, and the variable and true label of each voxel respectively be ω_i(or $\omega(x_i)$)$\in [1, K]$ and $\overline{\omega}_i \in [1, K]$, $1 \leq i \leq N$. Incorporating a multiplicative bias field b_i and an additive noise ρ, the image intensity y_i(or $y(x_i)$), $1 \leq i \leq N$, is modeled as:

$$y_i = b_i \sum_{k=1}^{K} \delta_i^k y_i^k + \rho, \text{ where } \delta_i^k = \begin{cases} 0 & \overline{\omega}_i \neq k \\ 1 & \overline{\omega}_i = k \end{cases} \tag{1}$$

In equation 1, $\delta_i^k y_i^k$ represents the component given by tissue k in the ideal image without influence from noise and IIH and we refer their sum $\sum_{k=1}^{K} \delta_i^k y_i^k$ as the *ideal image*. Here we don't assume any particular statistical form on the noise term. Equation 1 is our initial image model and will be gradually transformed to facilitate image segmentation.

The term y^k in equation 1 can be seen as an arbitrary function over the space domain governed by the constraints on the spatial relationship between near voxels. Generally, we think the constraints should consider *a priori* knowledge about the structure and geometry of the objects in the image as well as the inherent image properties related to the image acquisition process. In brain T1-weighted MR images, we consider *a priori* knowledge K_1 and K_2 and use the following first-order logic to describe a spatial constraint: any pair of near voxels from two adjacent tissues differ more than any pair of near voxels in one of the two tissues:

$$\begin{aligned} &\forall x_i, x_j \in \Omega \, \forall k \in [1, K] \, \exists T^k \in [0, 1) \\ &\qquad d(x_i, x_j) \leq p \Rightarrow \\ &(\overline{\omega}_i = k \wedge \overline{\omega}_j = k+1 \Rightarrow r(y_i^k, y_j^{k+1}) < T^k) \wedge \\ &(\overline{\omega}_i = \overline{\omega}_j = k \Rightarrow r(y_i^k, y_j^k) > \max(T^{k-1}, T^k)) \end{aligned} \tag{2}$$

$$r(a, b) = \begin{cases} a/b & a < b \\ b/a & a \geq b \end{cases} \tag{3}$$

In equation 2, T^0 and T^K are forced to be 0, $d(x_i, x_j)$ represents the distance between voxel x_i and x_j, and p is a distance threshold (a voxel cube is of unit dimension). Theoretically, any form of distance, including Euclidean distance, can be used. However, D^6, D^{18} or D^{26} distance is preferable because of the computational efficiency.

A reasonable assumption about the bias field is that it varies slowly across the space with respect to the intensity variation between different tissues in the ideal image. We use a first-order logic to describe this assumption in equation 4 without any constraints on the variation patterns.

$$\begin{aligned} &\forall x_i, x_j \in \Omega \, \exists \epsilon \in (0, 1) \\ &(1 - \epsilon \ll 1 - \max(T^1, ..., T^{K-1})) \wedge \\ &(d(x_i, x_j) \leq p \Rightarrow r(b_i, b_j) > \epsilon) \end{aligned} \tag{4}$$

Based on the low frequency property of the bias field, we can safely let the function y^k absorb the bias field function and the bias field term can thus be dropped from equation 1 while validity of the constraint in equation 2 is maintained. Therefore the image artifact of IIH is made transparent in our image model.

Next, we apply Gaussian filtering on the original gray level image to counteract the noise and drop the noise term from equation 1. Let $z = g(\sigma_z)$ be a specific blurred image. The new image model on z is:

$$z_i = \sum_{k=1}^{K} \delta_i^k z_i^k \tag{5}$$

Here, z^k corresponds to the contribution of tissue k to the blurred image. After Gaussian filtering, we want to maintain the spatial relationships between voxels, as described equation 6.

$$\begin{aligned} &\forall x_i, x_j \in \Omega \, \forall k \in [1, K] \, \exists T^k \in [0, 1) \\ &\qquad d(x_i, x_j) \leq p \Rightarrow \\ &(\overline{\omega}_i = k \wedge \overline{\omega}_j = k+1 \Rightarrow r(z_i^k, z_j^{k+1}) < T^k) \wedge \\ &(\overline{\omega}_i = \overline{\omega}_j = k \Rightarrow r(z_i^k, z_j^k) > \max(T^{k-1}, T^k)) \end{aligned} \tag{6}$$

It is well-known that Gaussian filtering blurs both homogeneous regions and edges. This leads to mainly two types of violation to the constraint. First, for a voxel pair (x_i, x_j) of different types on the opposite sides of an edge, if they are too close to each other, $r(z_i, z_j)$ may be significantly increased such that they may be identified as the same type. We think this adverse effect can be minimized by increasing the distance between voxels pairs for comparison in the relative thresholding procedure. The second type of violation may occur when the dimension of some parts of the structure of interest is too narrow compared to the Gaussian filter aperture (σ_z). We found that for current MRI techiques, the usual resolution (around $1mm^3$) is high enough so that this violation brings very little negative influence.

3.3 Applying Relative Thresholds

Given two relative thresholds T_{gw} between GM and WM, and T_{cg} between CSF and GM, we use two algorithms for the segmentation. The inputs to both include a *thresholding applying region* R, a *comparing image* h from which voxels are compared (we use z), a gradient graph G constructed on R, and a relative threshold. Based on the formulation of the *a priori* knowledge, we found that it suffices for the segmentation to compare only voxels pairs along paths in the gradient graph. Each comparison involves an objective voxel and a reference voxel. In algorithm 1, the reference voxel $ref_{gw}(v_i)$ for the object voxel v_i is of distance p from v_i along the path emanates from v_i. In algorithm 2, the reference voxel $ref_{cg}(v_i)$ for the object voxel v_i is the farthest GM vertex along the path emanates from v_i. We found that it gave slightly better results to temporarily change $h(ref_{cg}(v_i))$ to $h(ref_{gw}(ref_{cg}(v_i)))(1-(1-T_{gw})*2)$ for each comparison in algorithm 2. This is based on our observation that 1 minus the optimal threshold T^*_{gw} is roughly half of 1 minus the ratio between average GM and WM intensities.

It is easy to see that as long as our image model (formula 6) and the *a priori* knowledge in 3.1 are valid and optimal thresholds are given, the first algorithm guarantees the exact separation between GM and WM and the second algorithm guarantees the exact separation between CSF and GM. In practice, the segmentation accuracy depends on the goodness of the thresholds and the extent to which the image model and the *a priori* knowledge are valid.

Algorithm 1 GW-thresholding(R, h, G, T_{gw}).

initialization: $\forall x_i \in R\ \omega_i \leftarrow$WM;
for all $x_i \in R$ **do**
  if $\omega(ref_{gw}(x_i)) =$ GM **then**
    $\omega_i \leftarrow$ GM;
  else if $r(h_i, h(ref_{gw}(x_i))) < T_{gw}$ **then**
    $\omega_i \leftarrow$ GM;
  end if
end for

Algorithm 2 CG-thresholding(R, h, G, T_{cg}).

for all $x_i \in R$ s.t. $\omega_i =$ GM **do**
  if $r(h_i, h(ref_{cg}(x_i)) < T_{cg}$ **then**
    $\omega_i \leftarrow$ CSF;
  end if
end for

3.4 Finding Optimal Thresholds

The optimal thresholds are found in a trial-and-evaluation scheme, as illustrated in algorithm 3. Theoretically, the range for both thresholds are (0,1) and there are infinite candidate thresholds. But in practice, we found that it suffices to try thresholds that are multpilers of 0.01 in [0.75, 1) and [0.1, 1) for T_{gw} and T_{cg} respectively. The range of T_{gw} is selected based on our observation that 1 minus the optimal threshold T^*_{gw} is roughly half of 1 minus the ratio between average GM and WM intensities, which is typically greater than 0.5 in T1-weighted MR images.

The first input to the algorithm is the region of interest that contain significant amount of all three brain tissues and non-brain tissues as less as possible so that the disturbance to threshold searching is minimized. We will refer to this region as *threshold searching region* R_s. Other inputs include a comparing image h, used in the above two thresholding algorithms, an *evaluation image* l, used for segmentation evaluation, and a gradient graph G_s, constructed on R_s. We choose to use the original intensity image y as the evaluation image and the blurred image z as the comparing image. After the optimal thresholds are found, they are applied on a threshold applying region R_a with graph G_a constructed on R_a. R_s and R_a are obtained with a method described in section 6.

Algorithm 3 Threshold-searching(R_s, h, l, G_s).

for all candidate threshold T_{gw} **do**
  apply GW-thresholding(R_s, h, G_s, T_{gw});
  for all candidate threshold T_{cg} **do**
    apply CG-thresholding(R_s, h, G_s, T_{cg});
    evaluate the segmentation, record the best
  end for
end for
return the optimal threshold T^*_{gw} and T^*_{cg};

Segmentation is evaluated with an objective function J as defined in equation 7:

$$J = \sum_{x_i, x_j \in R_s} \varphi_{ij} |l_i - l_j| / \sum_{x_i, x_j \in R_s} \varphi_{ij}, \qquad (7)$$

where φ_{ij} is 1 if there is a path of length 2 in G_s from x_i to x_j, or 0 otherwise. Minimization of J encourages intensity uniformity and penalizes intensity difference between voxels of the same type.

It is helpful to understand the mechanism of relative thresholding by comparing the result from optimal thresholds and those from non-optimal thresholds. Figure 1(b) shows that over-low threshold T_{gw} globally makes the white matter too fat while figure 1(c) shows that over-high T_{gw} globally makes it too

thin. In either case, the GM/WM boundary drifts away the correct situation in different directions.

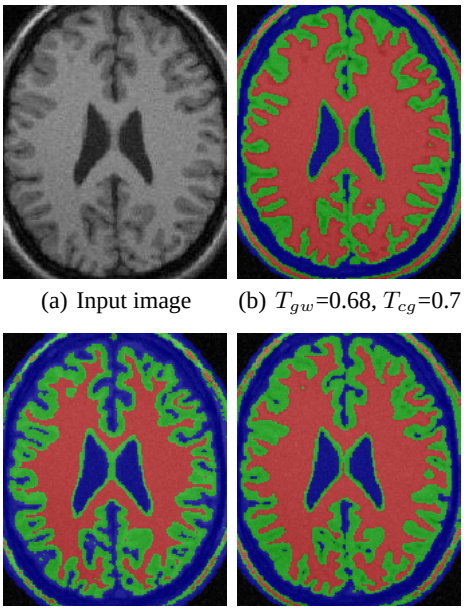

(a) Input image (b) T_{gw}=0.68, T_{cg}=0.7

(c) T_{gw}=0.93, T_{cg}=0.7 (d) T_{gw}=0.86, T_{cg}=0.7

Figure 1: Analysis of relative thresholding applied on a phantom image with optimal $T^*_{gw} = 0.86$ and $T^*_{cg} = 0.7$.

Due to various violation to our image model and *a priori* knowledge, segmentation errors arise even with optimal relative thresholds. A major error involves labeling non-brain voxels as brain voxels which are connected to the true brain voxels. This type of error will be corrected by morphological operations described in the next section. Another typical error is missing certain fine WM structures which are recovered with some ridge detection operations. Examples of such errors are circled in figure 3(b). The whole segmentation pipeline will be presented in section 5

4 MORPHOLOGICAL IMAGE ANALYSIS

In this section, we present the *skeleton-based opening* operation for eliminating false WM voxels and the *geodesic opening* operation for eliminating false GM and CSF voxels. Both operations are motivated by the *a priori* knowledge about the shape and geometry of brain structures. Before describing these two operations, we need to first have a review of geodesic dilation and geodesic erosion.

Geodesic dilation(erosion) (Soille, 2003) involves two input images: a marker image and a mask image. The geodesic dilation(erosion) of size 1 of the marker image f with respect to the mask image m is defined as the intersection(union) between m and the elementary dilation(erosion) of f. A usual constraint here is that the mask image m is the superset(subset) of the marker image f in geodesic dilation(erosion). The geodesic dilation(erosion) of size n of a marker image f with respect to a mask image m is obtained by performing n successive geodesic dilations(erosions) of size 1 of f with respect to m.

4.1 Skeleton-based Opening

Skeleton-based opening considers the characteristics of the special surface-like shape of the WM and the strong connectivity of the WM structure. It provides a large parameter range that gives rise to acceptable results. The main idea is that a special erosion and geodesic dilation are performed on the surface skeleton of the object instead of on the object itself. The algorithm consists of the following 5 steps.

1). Compute the reversible surface skeleton S of a 3D object by iterative thinning of the distance transforms with the method described in (Svensson, 2001). The skeleton is at most of two-unit thickness and is further thinned to two unit-thickness skeletons S_1 and S_2, where $S_1 \cup S_2 = S$, with the sub-iteration method described in (Borgefors et al., 1999).

2). Iteratively erode S_1 and S_2 based on the classification of the skeleton points. We use the method presented in (Saha and Chaudhuri, 1996) classifying the skeleton points into the following types: I(Isolated), SE(edge point of surfaces), S(inner point of surface), SS(junction point of surfaces), SC(junction point of surfaces and arcs), CE(arc end point), C(inner point of arcs), CC(junction point of arcs). In each iteration, a skeleton point is eroded only if its type is I, SE, CC, CE, C, or CC. The number of iterations n is taken as the parameter of the opening operation.

3). Find the largest components, C_1 and C_2, of the eroded skeletons respectively.

4). Compute the geodesic dilation of size n of C_1 and C_2 with respect to S_1 and S_2 respectively. The dilated skeletons are D_1 and D_2 respectively.

5). Recover the binary object from $D_1 \cup D_2$ by reverse distance transforms. Any voxels in the original object but not in the new object are discarded.

Our experiments of applying SBO on a set of WM groundtruths with resolution around $1mm^3$ demonstrated the following common behaviors of SBO: there are two parameter threshold d^1 (around 13) and d^2 (around 27) such that: 1) when $n < d^2$, all forebrain WM voxels remain almost intact in the result of SBO; 2) when $n > d^1$ the brainstem and cerebellum (BC) get dropped. Therefore, we can see that SBO provides two large parameter ranges for eliminating false WM voxels ($[1, d^1)$) and BC WM voxels

($[d^1, d^2)$) as long as the connectivity of the WM structure maintains well in the prior segmentation results.

4.2 Geodesic Opening

Geodesic opening also involves a marker image f and a mask image $m \subset f$. An example is that m denotes the WM voxel set and f denote the union of GM voxel set and m. Another example is that m denotes the union of GM and WM while f denotes the union of CSF, GM and WM. A geodesic opening of size n consists of three steps: a geodesic erosion of size n of f with respect to m resulting in image f_e, identifying the largest connected component f_c of f_e and eliminating any other components in f_e, and a geodesic dilation of size n of f_c with respect to f.

Geodesic opening has the effect of smoothing the geodesic distances of points in $f - m$ from m by eliminating protrusion voxels from f. Here, geodesic distance of a point v in $f - m$ from m is the minimum length of paths from v to m via only points in f. This smoothing effect is particularly helpful for elimination of unwanted structures from the initial GM and CSF voxel sets given by relative thresholding due to the following characteristics about GM and CSF structures: the thickness of human cortex is nearly uniform and CSF fills concave spaces forming a smooth boundary of the whole brain volume.

5 BRAIN MRI SEGMENTATION

In this section, we present the integration of RT and morphological operations into a whole brain MRI segmentation pipeline, as shown in figure 5. The pipeline starts with binarization of the input image and computing the threshold searching region (R_s) and the threshold applying region (R_a) from the foreground. We simply apply traditional thresholding with a threshold T_b for the binarization. The background intensities are modeled as a constant field a plus a noise term in Rayleigh statistics. The background pdf is thus $f(x|a,b) = ((x-a)/b^2)e^{-(x-a)^2/2b^2}$. The parameters of the pdf are estimated based on what we refer to as *automatic training*, which consists of following three steps. First, N_b voxels of lowest intensity in $g(\sigma_b)$ are selected as the training set. Second, the original intensities of the voxels in the training set are used as the sample data to estimate the parameter a^* and b^* that give rise to the maximum likelihood. Third, a threshold $T_b = a^* + 3b^*$ is applied on $y = g(0)$, $g(\delta)$, $g(2\delta)$, ..., $g(\sigma_b = n\delta)$ for the binarization resulting in a new training set of background voxels. Here, a voxel is taken as background if its intensity in any of $g(k\delta)|_{0 \le k \le n}$ is less than T_b. The second and third step can be repeated multiple times to get improved results.

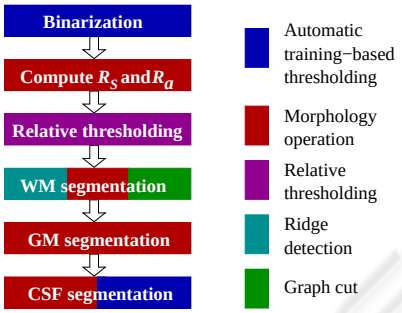

Figure 2: Segmentation pipeline.

We obtain a head mask image and take it as the threshold applying region R_a by applying SBO and morphology closing on the foreground. R_s is obtained by taking the intersection between the result of applying morphology erosion on R_a and those voxels within a distance d_s^1 from the superior end of the head. The erosion kernel ball radius d_s^2 is selected based on the *a priori* knowledge on skull thickness. A threshold searching region is shown in figure 3(a). A threshold applying region is shown in figure 3(b) as all colorful areas.

After T_{gw}^* and T_{cg}^* are found on R_s, apply them on R_a with the comparing image being $z = g(\sigma_z)$. Let S_w^z, S_g^z, S_c^z, denotes the result voxel set of WM, GM, and CSF respectively. We also use them to denote the corresponding mask images. An example of the result in shown in figure 3(b). Note that some missing fine WM structure are marked with cyan circles. Next, we use two ridge detection operations to recover these missing fine WM structures.

For each voxel $x_i \in S_g^z$, the first ridge detection operation checks the 26-neighborhood of x_i. Among all neighbor pairs of opposite direction from x_i, the pair (x_j, x_k) with maximum value of $|z_i - z_j| + |z_i - z_k|$ is selected. If $z_i > z_j$ and $z_i > z_k$, then x_i is taken as a WM ridge point, removed from S_g^z, and put into S_r. If $z_i < z_j$ and $z_i < z_j$, then x_i is taken as a valley point and put into S_v. Figure 3(c) shows the augmentation of WM ridge points.

The second operation depends on a *masked Gaussian filtering*. We use $\overline{g}(\sigma, m)$ to denote the result image of applying masked Gaussian filtering on the input image y with standard deviation σ and mask image m. Only voxels in the mask are filtered and any voxels outside the mask are not counted in the convolution calculation. A *masked Laplacian filtering* is then performed on $\overline{z} = \overline{g}(\sigma_z, S_w^z \cup S_g^z - S_v)$ with mask $S_g^z - S_v$ to recover more missing WM voxels. The Laplacian of each voxel $x_i \in S_g^z - S_v$ is $\sum_{x_j \in \mathcal{N}^6(x_i) \wedge x_j \in S_w^z \cup S_g^z - S_v} (\overline{z}_j - \overline{z}_i)$. If the laplacian

value is less than 0, x_i is taken as a WM ridge point, removed from S_g^z, and put into S_{lr}. The Laplacian ridge points are mainly used to enhance the connectivity of the WM structure and may incorporate many false WM voxels. They will be eliminated as the final step of WM segmentation.

We apply SBO on $S_w^z \cup S_r \cup S_{lr}$ with parameter d_w^1 resulting in a WM set S_w^1 with non-brain voxels removed. The same operation is performed with a greater parameter d_w^2 resulting in S_w^2 with further removement of brainstem and cerebellum(BC). Then we get the forebrain WM set as S_w^f by subtracting the largest component in $S_w^1 - S_w^2$ from S_w^1 and the BC WM set as $S_w^{bc} = S_w^1 - S_w^f$. Result of applying SBOs is illustrated in figure 3(d).

The separation between forebrain WM and BC WM is calibrated by a graph-cut based method. First we construct a grid graph in 26-connectivity from S_w^1. Then all vertices in S_w^{bc} are contracted into a source terminal and all vertices in S_w^f that are of geodesic distance greater than a threshold d_f from S_w^{bc} are contracted into a sink terminal. Finally we compute the minimum graph cut between the source and sink terminal. It is demonstrated in (Boykov and Kolmogorov, 2003) that as long as the edge weights in the grid graph are set to be inversely proportional to their length, the graph cut can approximate the area of the cut surface. In this way, the initial forebrain/BC separation is substituted with a smaller and more regular cut surface and S_w^f and S_w^{bc} are updated accordingly. Finally, we remove Laplacian ridge points by subtracting S_{lr} from S_w^f. All discarded WM voxels from S_w^z that have a path in G_a to S_w^f or S_w^{bc} are degraded to S_g^z. Final result of WM segmentation is shown in figure 3(e).

Given the result of WM, GM segmentation is made easier considering the *a priori* knowledge on the nearly uniform cortex thickness. First, we obtain an initial forebrain GM set $S_{ig}^f \subset S_g^z$ by extracting all voxels in S_g^z that have a path to S_w^f in G_a of length less than d_g^1. In a similar way, we can get the BC GM voxel set S_g^{bc} and the total BC set $S^{bc} = S_g^{bc} \cup S_w^{bc}$. False GM voxels in S_g^f are removed by a series of geodesic openings with size being 1, 2, ..., d_g^1. Let the result be S_g^f. These operations may over-smooth the geodesic distances of GM voxels to the WM set. We improve the result by simply computing the geodesic dilation of size $d_g^2 \ll d_g^1$ of S_g^f with respect to S_{ig}^f. Any discarded WM voxels from S_{ig}^f that have a path in G_a to S_w^f are degraded to CSF and put into S_c^z.

To improve the CSF voxel set given by relative thresholding, we first extract the subset $S_c \subset S_c^z$ in which each voxels has a path in G_a to $S_g^f \cup S_w^f \cup S^{bc}$. From S_c we build a normal distribution for CSF voxel intensities using a similar automatic training method to that used for image binarization (see the first paragraph of this section). The distribution then guides incorporation of additional CSF voxels. The updated CSF voxel set S_c is finally processed by a series of geodesic openings smoothing the brain volume boundary. A example of final result is shown in figure 3(f) and two real image segmentation results are shown in figure 4.

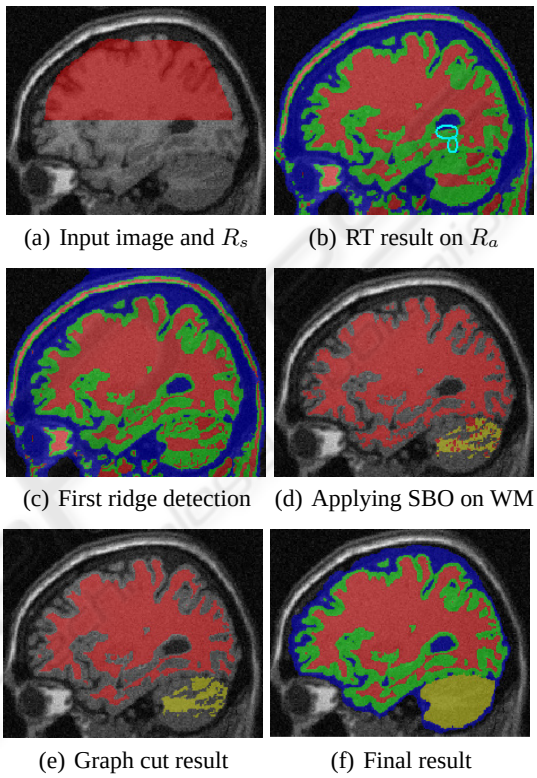

(a) Input image and R_s (b) RT result on R_a

(c) First ridge detection (d) Applying SBO on WM

(e) Graph cut result (f) Final result

Figure 3: Segmentation of a phantom brain (IIH level = 40%, noise level = 9%). WM, GM, CSF, and BC are colored with red, green, blue, and yellow respectively.

6 RESULTS

We have tested the segmentation algorithm against a set of phantom brains as well as 6 real images from 4 subjects scanned at 3 different MR machines. Some examples of the results are shown in figure 4. The resolution of the images are between $1.3mm^3$ and $1mm^3$. The average running time is less than 8 minutes on a single 1.3GHz Power4 processor. Searching for the optimal relative thresholds takes about 1.5 minutes. We use exactly the same set of parameters for all these images. Some important parameters are selected as follows: $\sigma_z = 1$, $\sigma_\nabla = 2$, $p = 8$, $d_s^1 = 95$, $d_s^2 = 25$, $d_w^1 = 4$, $d_w^2 = 18$, $d_g^1 = 15$, and $d_g^2 = 2$. We think this set of parameters work

for all input images with resolutions around $1mm^3$, which is typical for current MR techniques. The only place where user intervention may be needed is determining the transaxial dimension and the superior side to obtain the threshold searching region. This information can also be obtained by computation or from the input file.

To evaluate segmentation, we use a metric *overlap*, same as the Tanimoto coefficient (Duda and Hart, 1973), comparing two segmentations for a given voxel type labeling as the sum of voxels that both have the same label in each segmentation divided by the sum of voxels where either segmentation has the label. Table 1 list the overlaps of WM and GM respectively between the groundtruth and our results on phantom brains corrupted with partial volume effect, various levels of IIH and noise (Cocosco et al., 1997). The noise level represents the percent ratio of the standard deviation of the white Gaussian noise versus the signal for a reference tissue. For a IIH level x, the multiplicative IIH field has a range of values of $1-x...1+x$ over the brain area.

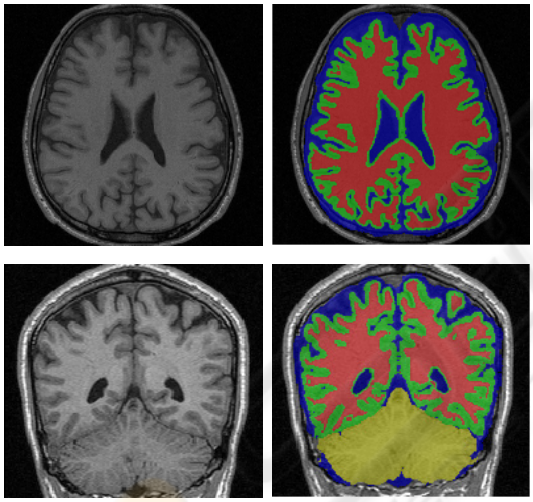

Figure 4: Results of two real images.

7 CONCLUSION

We have demonstrated a new automatic brain MRI segmentation method with relative thresholding and morphological operations. Relative thresholding makes IIH transparent and allows global searching for optimal solutions. Prior skull stripping is not required. Parameters are selected based on *a priori* knowledge and are robust to inter-data variations.

Table 1: WM and GM overlaps on a set of phantom brains.

Type	IIH	N=3%	N=5%	N=7%	N=9%
WM	20%	.8931	.8899	.8897	.8812
WM	40%	.8926	.8899	.8832	.8824
GM	20%	.8100	.8043	.8060	.7967
GM	40%	.8074	.8060	.8048	.7996

REFERENCES

Ahmed, M. N. et al. (2002). A modified fuzzy c-means algorithms for bias field estimation and segmentation of mri data. *IEEE Trans. Medical Imaging*, 21(3).

Borgefors, G. et al. (1999). Computing skeletons in threee dimension. *Pattern recognition*, 32(7).

Boykov, Y. and Kolmogorov, V. (2003). Computing geodesics and minimal surfaces via graph cuts. In *International Conference on Computer Vision*.

Cocosco, C. A. et al. (1997). Brainweb: Online interface to a 3d mri simulated brain database. *NeuroImage*, 5(4).

Cohen, M. S. et al. (2000). Rapid and effective correction of rf inhomogeneity for high field magnetic resonance imaging. *Human Brain Mapping*, 10.

Duda, R. and Hart, P. (1973). *Pattern Classification and Scene Analysis*. Wiley, New York.

MacDonald, D. et al. (2000). Automated 3-d extraction of inner and outer surfaces of cerebral cortex from mri. *NeuroImage*, 12(3).

Pham, D. L. and Prince, J. L. (1999). An adaptive fuzzy c-means algorithm for image segmentation in the presence of intensity inhomogeneities. *Patt. Rec. Let.*

Rehm, K. et al. (04). Putting our heads together: a consensus approach to brain/non-brain segmentation in t1-weighted mr volumes. *NeuroImage*, 22.

Saha, P. K. and Chaudhuri, B. B. (1996). 3d digital topology under binary transformation with applications. *Computer vision and image understanding*, 63(3).

Sled, J. G. et al. (1998). A nonparametric methods for automatic correction of intensity nonuniformity in mri data. *IEEE Trans. Medical Imaging*, 17.

Soille, P. (2003). *Morphological image analysis*. Springer-Verlag.

Svensson, S. (2001). Reversible surface skeletons of 3d objects by iterative thinning of distance transforms. In *G.Bertrand et al. (Eds.): Digital and Image geometry, LNCS 2243*.

Wells, W. M. et al. (1998). Adaptive segmentation of mri data. *IEEE Trans. Medical Imaging*, 15.

Xu, C. Y. et al. (1999). Reconstruction of the human cerebral cortex from magnetic resonance images. *IEEE Trans. Medical Imaging*, 18.

Zeng, X. et al. (1999). Segmentation and measurement of the cortex from 3-d mr images using coupled-surfaces propagation. *IEEE Trans. Medical Imaging*, 18(10).